Supporting Information

for

Investigation of Charge-transfer between 4-Mercaptobenzoic Acid Monolayer and TiO_2 Nanoparticles under High-Pressure Using Surface-enhanced Raman Scattering

Peng Li[a], Xiaolei Wang[a], Haiyan Li[b], Xuwei Yang[c], Xiaolei Zhang[a], Lixia Zhang[c], Yukihio Ozaki[d], Bingbing Liu[b]*, and Bing Zhao[a]*

[a]Stake Key Laboratory for Supramolecular Structure and Materials, Jilin University, Changchun 130012, China

[b]State Key Lab Superhard Materials,Jilin University, Changchun 130012, China

[c]College of Chemistry, Jilin University, Changchun 130012, China

[d]Department of Chemistry, School of Science and Technology, Kwansei Gakuin University, Sanda, Hyogo 669-1337, Japan

E-mail: zhaob@mail.jlu.edu.cn liubb@jlu.edu.cn

Experimental Procedures

Chemicals. 4-Mercaptobenzoic acid (4-MBA) was purchased from Sigma-Aldrich and used without further purification. All other chemicals were acquired from Beijing Chemical Reagent Factory and used without further purification. The distilled and deionized water from a Milli-Q-plus system with resistivity >18.0 MΩ was used in aqueous solutions.

Synthesis of TiO_2 NPs. TiO_2 NPs were prepared using a sol-hydrothermal process.[1] First, a mixed solution of 15 mL of tetrabutyl titanate and 15 mL of anhydrous ethanol was added dropwise into another mixed solution consisting of 60 mL of anhydrous ethanol, 15 mL of water, and 3 mL of 70% nitric acid, at 23–28°C under rough stirring to carry out hydrolysis. Subsequently, yellowish transparent sol was obtained by continuous stirring for 2 h. The as-prepared sol was kept at 160°C for 6 h in a stainless-steel vessel, and then cooled to room temperature. The sol-hydrothermal production was dried at 80°C for 6 h. Finally, TiO_2 NPs were obtained by calcining the TiO_2 sol-hydrothermal production for 2 h at 350, 400, 450, 500, 550, 600, and 800°C, respectively.

Adsorption of Probing Molecules. TiO_2 nanocrystals surface-modified by molecules were obtained as follows: 20 mg of TiO_2 nanocrystals were dispersed in 20 mL of 4-MBA (1×10^{-3} M) ethanol solution, and the mixture was stirred for 6 h. Then, the precipitate was centrifuged and rinsed with purified water once more. Finally, after drying, TiO_2 NPs modified by a 4-MBA molecular monolayer were obtained.

Preparation for High-Pressure Experiments. High-pressure experiments were carried out in a diamond anvil cell (DAC). A 50-μm-thick T301 stainless steel gasket with a 100-μm diameter hole was used to load the samples between diamonds having 300-μm cults. Liquid argon was used as the pressure transmitting medium (PTM) to enable hydrostatic conditions. The pressures were measured by the ruby fluorescence technique.

Sample Characterization. The crystalline structure of the TiO_2 sample was determined by X-ray diffraction using a Siemens D5005 X-ray powder diffractometer with a Cu Kα radiation source at 40 kV and 30 mA. The UV-Vis DRS spectra were recorded on a PerkinElmer Lambda950 UV-Vis-NIR spectrophotometer. TEM images were taken using a JEM-2100F high-resolution transmission electron microscopy operating at 200.0 kV.

Raman spectra were obtained by a Horiba-Jobin Yvon LabRAM ARAMIS system with a spectral resolution of ca. 4 cm^{-1}; The 633-nm radiation from a 20-mW air-cooled HeNe narrow bandwidth laser was used as an exciting source. The laser beam was focused onto a spot with a diameter of approximately 1 μm using an objective microscope with a magnification of 50×. The Raman band of the silicon wafer at 520.7 cm^{-1} was used to calibrate the spectrometer. Data acquisition was the result of two times 10-s accumulations for the 4-MBA molecules absorbed on TiO_2 NPs at ambient temperature and pressure; Moreover, the results of the system under high pressure were acquired one time 60s accumulations by a HORIBA LabRAM HR Evolution microscope Raman spectrometer and the laser excitation wavelength used was 532 nm.

Results and Discussion

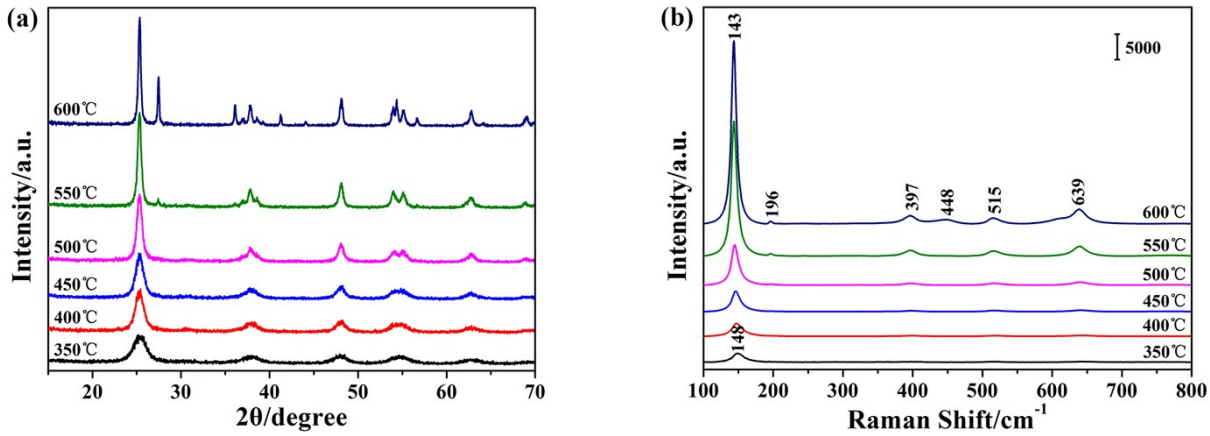

Figure S1. (a) XRD patterns and (b) Raman spectra of pyrogenic TiO_2 NPs under different calcinated temperatures.

XRD was used to identify the size and structure of TiO_2 NPs. The crystalline structure of the TiO_2 NPs was determined according to the XRD peaks at 25.3° (JCPDS 71-1166) and 27.4° (JCPDS 73-2224), which are identified as anatase and rutile crystalline phase of TiO_2,

respectively. When we calculated the particle size of TiO_2 NPs using the XRD, it was found that the intensity of diffraction peaks increases, and they become narrower as the calcination temperature increases from 350 to 600°C, indicating that both the degree of crystallinity of samples and the crystalline size increase. These sizes were estimated from the half band-width of the XRD peak using the Scherrer formula: $D=k\lambda/(\beta\cos\theta)$, where λ is the X-ray wavelength, β is the half width of the (110) peak, θ is the Bragg diffraction angle, and k is a correction factor, which was taken as 0.89.[2] The results has been shown in main body of the paper.

Ohsaka et al. reported that TiO_2 contains 15 irreducible representations of optical vibrational modes: $1A_{1g}+1A_{2u}+2B_{1g}+1B_{2u}+3E_g+2E_u$. The vibrational modes of A_{2u} and E_u are infrared active, while those of A_{1g}, B_{1g}, and E_g are Raman active. Figure S1b shows the Raman bands of TiO_2 NPs, all peaks are anatase-phase TiO_2 when the calcination temperature was below 550℃, a weak peak characteristic of the rutile phase TiO_2 appears at 448 cm^{-1},when the calcination temperature were 550 and 600℃. Moreover, it can be seen from Figure 1b that the Raman peaks shift toward lower wavenumbers (note, the shift from 148 cm^{-1} to 143 cm^{-1}), and that their intensities increase as the particle size of TiO_2 NPs increases. These results are comparable to those previously obtained by Xue[3] and Swany et al.[4] for anatase nanocrystals of TiO_2. With respect to the degree of crystallinity, it should be noted that the intensity of phonon vibrational modes of TiO_2 in the region of 800–100 cm^{-1} increases as the calcination temperature increases.

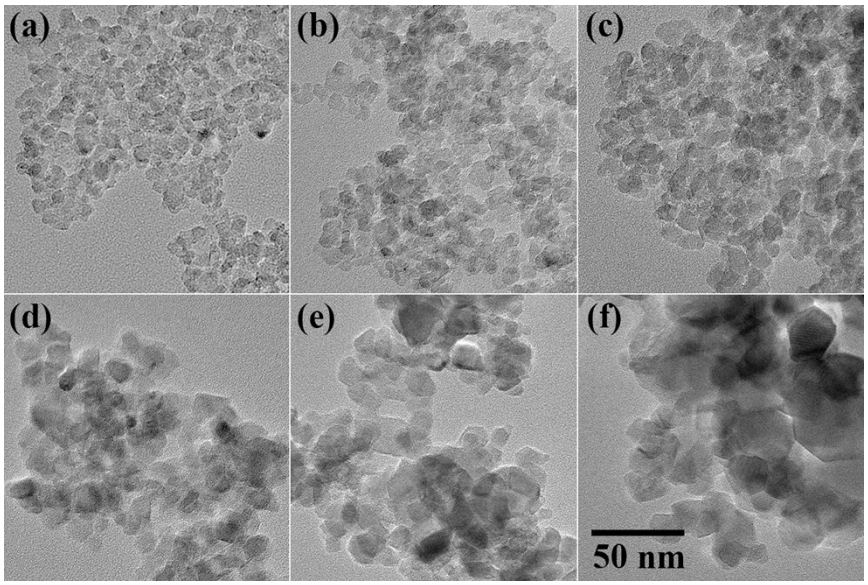

Figure S2. TEM images of TiO_2 NPs obtained by calcining at different temperatures, (a) 350, (b) 400, (c) 450, (d) 500, (e) 550, and (f) 600°C.

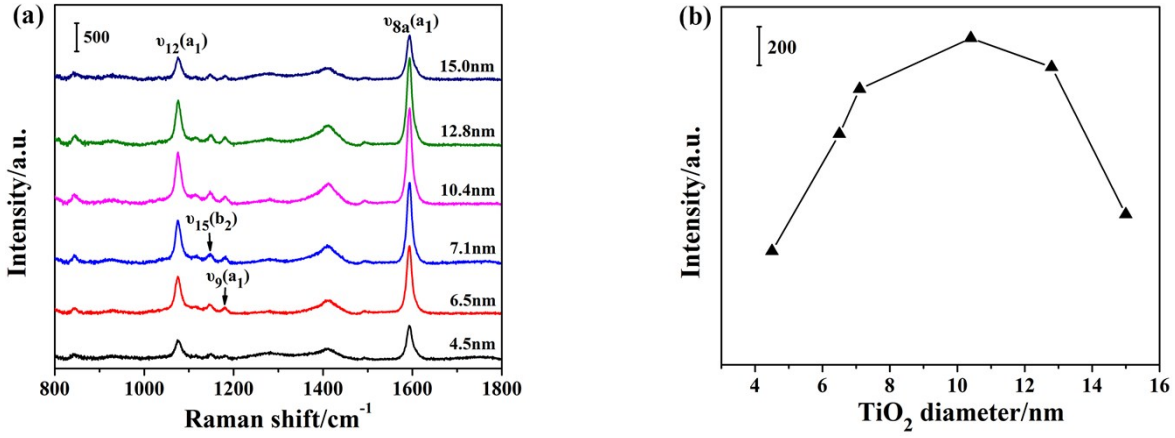

Figure S3. (a) SERS spectra of 4-MBA adsorbed on TiO_2 NPs with various sizes from a 1×10^{-3} M ethanol solution under ambient pressure. (b) SERS intensity of the 1594 cm^{-1} band versus the size of TiO_2 NPs.

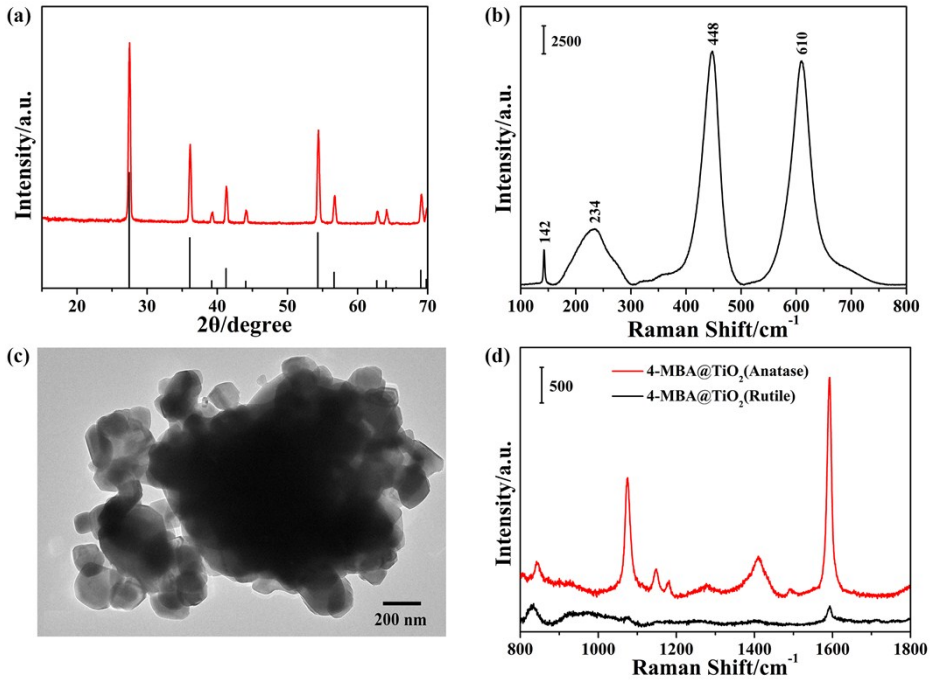

Figure S4. (a) The XRD patterns (b) Raman spectrum and (c) TEM image of rutile phase TiO_2 NPs, (d) The SERS spectra of 4-MBA adsorbed on anatase and rutile phase TiO_2 NPs at ambient.

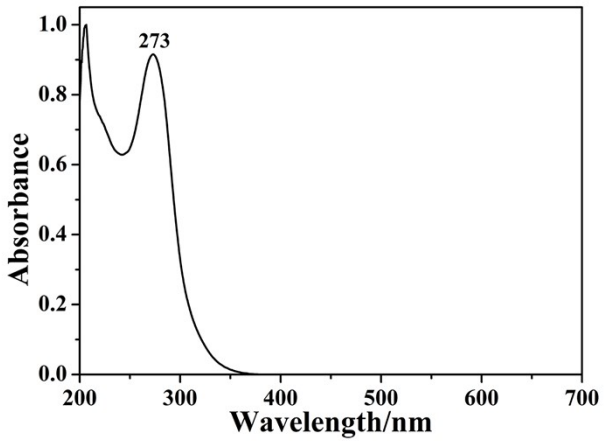

Figure S5. The UV absorption spectrum of 4-MBA ethanol solution, and the solution concentration is 1×10^{-5} M.

In order to further explain why the anatase phase TiO_2 NPs was chosen as the substrate to explore the high pressure SERS, a comparative experiment was conducted, and the results shown in Figure S4. The rutile phase TiO_2 NPs were obtained by calcining the TiO_2 sol-hydrothermal production for 2 h at 800°C. As shown in Figure S4a and S4b, the XRD (JCPDS 73-2224) and the Raman[5] results all show that this TiO_2 NPs are pure rutile phase TiO_2. According to the Figure S4c, the rutile phase TiO_2 NPs are quasi-spherical and dispersed homogeneously, the particles size was about 175–210 nm. Moreover, the SERS spectra of 4-MBA adsorbed on the antase (500°C) and rutile (800°C) phase TiO_2 NPs at ambient were obtained, as shown in Figure S4d, and the SERS signal of 4-MBA adsorbed on the rutile phase TiO_2 NPs is fairly weak compared with the antase phase TiO_2 NPs. Therefore, the anatase phase TiO_2 was used as an active-substrate in the high pressure SERS experiments rather than the rutile phase TiO_2.

Figure S5 displays an UV absorption spectrum of 4-MBA ethanol solution. The characteristic absorption peak of 4-MBA is located at 273 nm, and there is no absorption peak in the visible region. No resonance occurred between 4-MBA and the visible laser used in this work. Therefore, the research method we used is SERS rather than resonance Raman scattering.

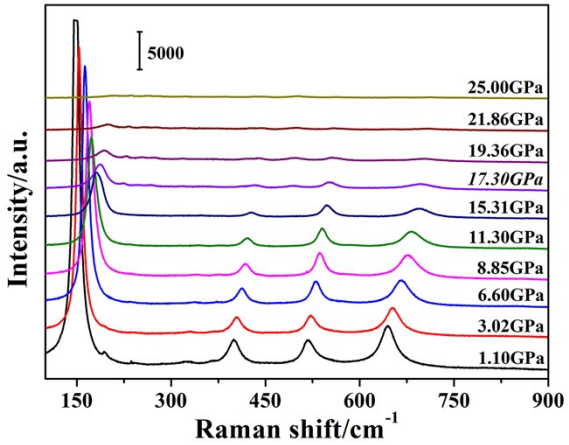

Figure S6. Raman spectra of TiO_2 NPs with adsorbed 4-MBA measured in the pressure range of 1.10-25.00 GPa.

In order to determine the effects of high pressure on TiO_2 NPs and 4-MBA solid powder, we performed a series of experiments. Figure S6 shows the Raman spectra of TiO_2 NPs with 4-MBA adsorbed obtained in the range of 1.10–25.00 GPa. We can easily observe that all the Raman peaks shift to higher wavenumbers, and that their intensities decrease with the increase in the pressure. The pressure-induced blue shift of Raman peaks is the most common phenomenon associated with the increased density in molecular systems, and has been discussed in detail in many works[6-8]; the high pressure can shorten bond lengths and increase the force constant and frequency of the corresponding peak[5,9], causing the blue shifts. The reason for the decrease in the intensity is that the phonon vibrations are restrained by the high pressure that is applied, and it is a common phenomenon in studies of high pressure[10-13]. We should also verify that no phase changes are taking place during the process of increasing the pressure until about 17.30 GPa (See Figure S8); the result of the phase-transformation point is consistent with those of other studies[10-13].

Raman spectra of 4-MBA solid powder under high pressure are shown in Figure 2c. In this experiment, the range of pressure was from 1.92 to 21.00 GPa. It can be seen from Figure 2c that Raman bands also show a blue shift for this system. The reasons for these shifts are mainly due to the shortening of the bond lengths in the 4-MBA molecules. When the system is subjected to high pressure, the bond lengths of all bonds in the molecules are shortened, the frequency of the corresponding band increases, and blue shifts of Raman peaks then occur. Another significant observation is that the intensity increases in the Raman peak at 1610 cm^{-1} as the pressure increases up to about 2.64 GPa, and it then decreases. There are two possible factors that affect the intensity of the Raman peak at 1610 cm^{-1}, namely the decrease of the molecular spacing and the destruction of the crystalline structure. When a pressure below 2.64 GPa was applied, the decrease in the molecular spacing is a dominant factor. The high pressure may decrease the molecular spacing, and hence, there is an increase in the number of molecules under the laser light spot as the pressure increases. If the laser spot size remains the same, the Raman signal becomes stronger. During the next stage, the excessive pressure damages the crystalline structure of 4-MBA, and the intensity of the Raman peak decreases.

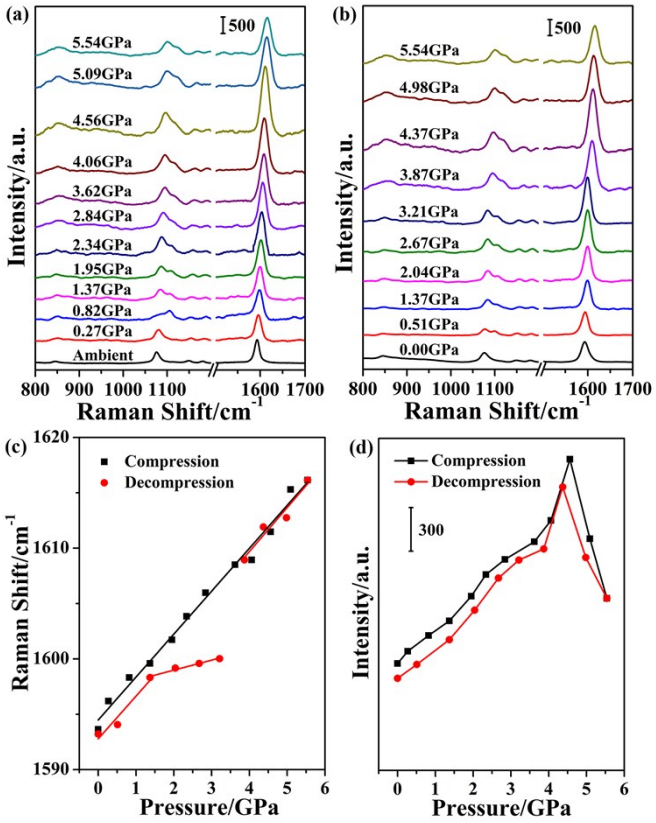

Figure S7. High pressure SERS spectra of the 4-MBA@TiO_2 system during (a) compression, and (b) decompression cycle in the pressure range of 0-5.54 GPa, (c) a plot of frequencies of the Raman active band (1594 cm^{-1}) versus the pressure, (d) a plot of the SERS intensity of the 1594 cm^{-1} band of 4-MBA versus pressure.

The compression and decompression experiments for the 4-MBA@TiO_2 system below 5.54 GPa were shown in Figure S7. The results show that the shift and intensity change of Raman peaks were approximately reversible. During the compression cycle, the Raman shift of 1594 cm^{-1} band show approximately linear pressure inducecd blue shift, and the slope is 3.87 cm^{-1}/GPa. During the decompression cycle, with the decrease in the pressure, the Raman band shift towards lower wavenumbers in whole range, there are some differences in the linear slopes: in the range of 5.54–3.87 GPa, the slope is 3.97 cm^{-1}/GPa; in the range of 3.21–1.37 GPa, the slope is 0.90 cm^{-1}/GPa; and in the range of 1.37–0 GPa, the slope is 3.86 cm^{-1}/GPa. On the whole, according to Figure S7c, the Raman peak come back to original wavenumber by decreasing pressure from 5.54 GPa to ambient, and the significant decrease in slope in the range of 3.21–1.37 GPa is probably because that the molecular bond length changes are relatively insensitive to pressure in this range. For the changes in the intensity of 1594 cm^{-1} band, as shown in Figure S7d, the variation trend of the intensity are basically consistent during the compression and decompression cycle; the difference is only that the peak intensity in the decompression cycle is slightly lower than that in the compression cycle, and the reason may be that the pressure has caused a minor damage to the molecules.

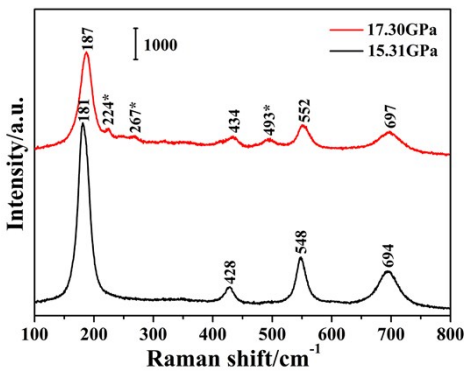

Figure S8. Raman spectra of TiO_2 NPs obtained under the pressure of 15.31 and 17.30 GPa, respectively.

From Figure S8, we can see that new peaks (with * symbol) appear when the pressure becomes 17.30 GPa. The appearance of the new peaks indicates that pressure-induced phase transition occurs, i.e., the TiO_2 NPs in our experiments had a signal phase when the pressure fell below 17.30 GPa.

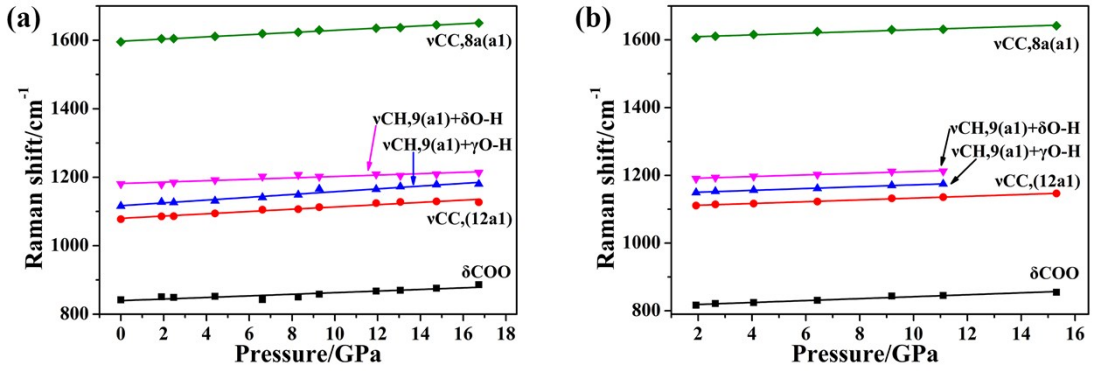

Figure S9. Plots of frequencies of the Raman active bands versus the pressure. (a) 4-MBA monolayer adsorbed on TiO_2 NPs. (b) 4-MBA solid powder.

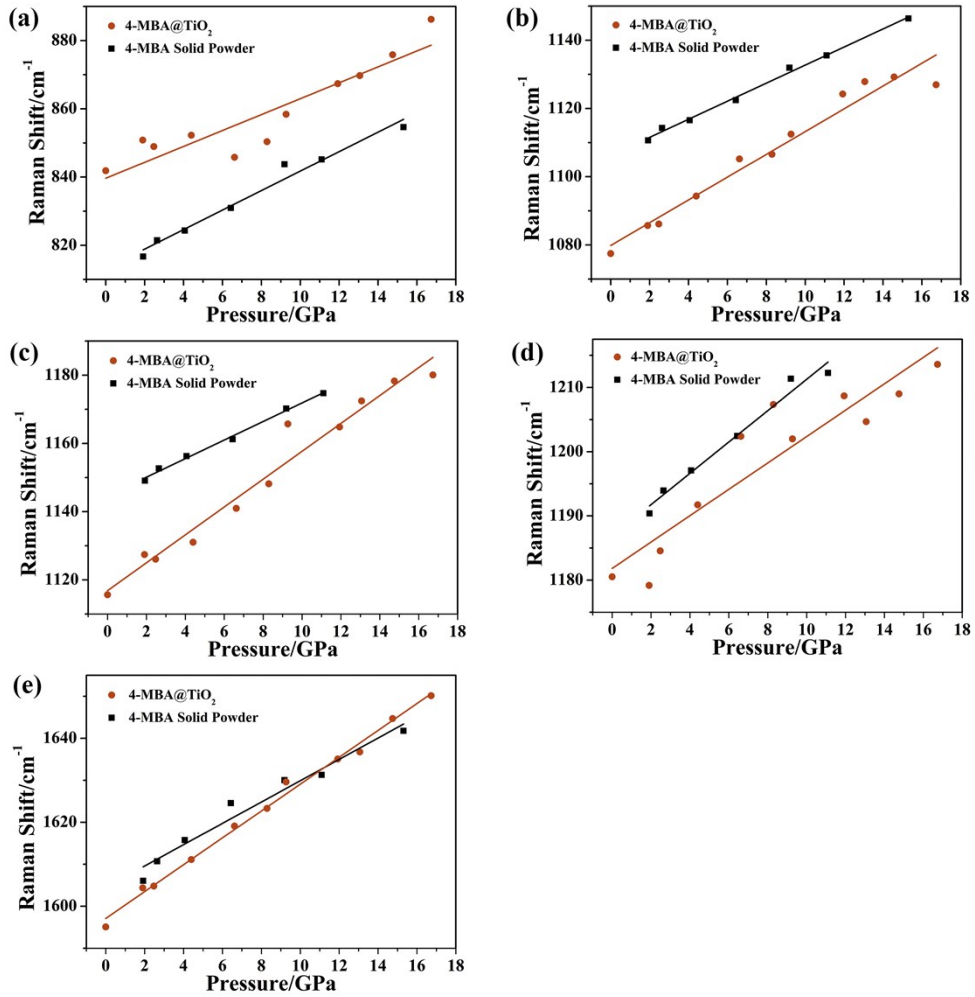

Figure S10. Comparison of pressure-induced blue-shifts of 4-MBA monolayer adsorbed on TiO_2 NPs (SERS date, read dot) and a solid powder (black square), (a) δOCO band, (b) υCC,12(a1) band, (c) υCH,9(a1)+γO-H band, (d) υCH,9(a1)+δO-H band, and (e) υCC,8a(a1) band.

As shown in Figure S9, the Raman shifts of all the bands of the 4-MBA monolayer adsorbed on TiO_2 NPs and 4-MBA solid powder show approximately linear dependent changes on the pressure. No inflection points appear for the whole range of pressure, indicating that no phase transitions occurred. With the increase in the pressure, all of the bands shift towards higher frequencies at different slopes for 4-MBA monolayer adsorbed on TiO_2 NPs and solid powder. The slopes of δOCO; υCC,12(a1); υCH,9(a1)+γO-H; υCH,9(a1)+δO-H and υCC,8a(a1); bands for the 4-MBA monolayer adsorbed on TiO_2 NPs are 2.33, 3.34, 4.08, 2.05, and 3.20 cm^{-1}/GPa, respectively. The slopes of δOCO; υCC,12(a1); υCH,9(a1)+γO-H; υCH,9(a1)+δO-H; and υCC,8a(a1) bands for 4-MBA solid powder are 2.86, 2.65, 2.72, 2.44, and 2.54 cm^{-1}/GPa, respectively. It is obvious that the effects of the pressure on the Raman shifts for all the bands of 4-MBA solid powder are almost uniform, and the pressure-induced blue shift for each band of the 4-MBA monolayer adsorbed on TiO_2 NPs is slightly different. As shown in Figure S10 for pressure-induced blue shifts of the 4-MBA monolayer on TiO_2 NPs and a solid powder, for each band, there are different high-pressure behaviors for the 4-MBA monolayer adsorbed on TiO_2 NPs and solid powder. According to Figure S10, the formation of a 4-MBA monolayer can suppress the degree of pressure-induced blue shift for bending or deformation bands (δOCO; υCH,9(a1)+δO-H) compared to solid powder. In contrast, the pressure-induced blue shift of stretching bands (υCC,12(a1); υCC,8a(a1)) and the rocking bands (υCH,9(a1)+γO-H) are more sensitive for the 4-MBA monolayer adsorbed on TiO_2 NPs. Besides, the degree of the pressure-induced blue shift for the rocking bands is the most sensitive in all bands of the 4-MBA monolayer adsorbed on TiO_2 NPs. It should be noted that higher frequency shifts of all the bands of the 4-MBA monolayer adsorbed on TiO_2 NPs and solid powder confirm that the blue shift of Raman peaks in the 4-MBA@TiO_2 system is not due to the phase transition of TiO_2 NPs (In fact, there is no phase transition occurring for the entire process).

Table S1. Wavenumbers and assignments of a Raman spectrum of anatase phase TiO_2 NPs.

Vibrational mode	$E_{g(1)}$	$E_{g(2)}$	$B1_{g(1)}$	A_{1g}	$B1_{g(2)}$	$E_{g(3)}$
Raman shift/cm^{-1}	148	196	397	515	519	639

Table S2. Wavenumbers (cm^{-1}) and assignments of bands in the Raman and SERS spectra of 4-MBA molecule.

Raman Bulk	SERS on TiO_2	Assignment
1596	1594	υCC,8a(a_1)
1451	1493	υCC+δCH
1405	1412	υCOO–
1182	1182	υCH,9(a_1)+ δO-H
	1148	υCH,15(b_2)
1136	1116	υCH,9(a_1)+ γO-H
1098	1078	υCC,12(a_1)
913		δCSH,9b(b_2)
813	843	δOCO

Note: δ-bending or deformation vibration; ν-stretching vibration; γ-rocking vibration.

Table S3. The E_g values of TiO_2 NPs under various pressure calculated by equation (2).

P/GPa	0	1.90	2.47	4.40	6.62	8.29	9.27	11.93	13.06	14.75	16.73
E_g/eV	3.270	3.253	3.248	3.231	3.212	3.197	3.188	3.165	3.155	3.140	3.123

References

1. L. Yang, X. Jiang, W. Ruan, B. Zhao, W. Xu, J. R. Lombardi, *J. Phys. Chem. C,* 2008, **112**, 20095.
2. V. Swamy, B. C. Muddle, Q. Dai, *Appl. Phys. Lett.,* 2006, **89**, 116118.
3. X. Xue, W. Ji, Z. Mao, H. Mao, Y. Wang, X. Wang, W. Ruan, B. Zhao, J. R. Lombardi, *J. Phys. Chem. C,* 2012, **116**, 8792.
4. V. Swamy, A. Kuznetsov, L. S. Dubrovinsky, R. A. Caruso, D. G. Shchukin, B. C. Muddle, *Phys. Rev. B,* 2005, **71**, 184302.
5. J. Zhang, M. J. Li, Z. C. Feng, J. Chen and C. Li, *J. Phys. Chem. B*, 2006, **110**, 927.
6. J. Jiang, H. Li, L. Dai, H. Hu, C. Zhao, *AIP Adv.,* 2016, **6**, 035214.
7. K. Pereira da Silva, M. Ptak, P. S. Pizani, J. Mendes Filho, F. E. A. Melo, P. T. C. Freire, *Vib. Spectrosc.,* 2016, **85**, 97.
8. Y. Ren, X. Cheng, K. Yang, X. Zhu, H. Li, Y. Wang, *J. Mol. Struct.,* 2015, **1102**, 6.
9. G. R. Hearne, J. Zhao, A. M. Dawe, V. Pischedda, M. Maaza, M. K. Nieuwoudt, P. Kibasomba, O. Nemraoui, J. D. Comins, M. J. Witcomb, *Phys. Rev. B,* 2004, **70**, 134102.
10. T. Arlt, M. Bermejo, M. A. Blanco, L. Gerward, J. Z. Jiang, J. S. Olsen, J. M. Recio, *Phys. Rev. B,* 2000, **61**, 14414.
11. X. Lu, W. Yang, Z. Quan, T. Lin, L. Bai, L. Wang, F. Huang, Y. Zhao,. *J. Am. Chem. Soc.,* 2014, **136**, 419.
12. V. Swamy, A. Kuznetsov, L. S. Dubrovinsky, P. F. McMillan, V. B. Prakapenka, G. Shen, B. C. Muddle,. *Phys. Rev. Lett.,* 2006, **96**, 135702.
13. Y. Huang, F. Chen, X. Li, Y. Yuan, H. Dong, S. Samanta, Z. Yu, S. Rahman, J. Zhang, K. Yang, S. Yan, L. Wang, *J. Appl. Phys.,* 2016, **119**, 215903.